*Chapter 3*

# TOWARDS IMAGING FLUORESCENLY LABELED PROTEINS WITH TIP-ENHANCED FLUORESCENCE MICROSCOPY (TEFM)

In collaboration with the Quake group of Caltech, we demonstrated sub-10 nm optical resolution with a Tip-Enhanced Fluorescence Microscope (TEFM) imaging quantum dots[1] and single-molecules[2] on a dry surface. TEFM is a hybrid microscope that combines an Atomic Force Microscope (AFM) with a custom Total Internal Reflection Fluorescence Microscope (TIRFM). A 543 nm excitation laser beam is focused through a microscope objective at the top surface of a glass coverslip to stimulate an evanescent field. Emitted fluorescence is collected by the microscope objective and then directed onto an avalanche photodiode (APD) through a system of spectral filters. In Figure 3-1 the major components in a TEFM are shown schematically. The two patents awarded for this microscope are Appendices C and D.

After joining the Scott Fraser group this instrument was substantially enhanced to enable imaging of proteins in a biologically relevant warm, wet environment. In collaboration with the Henry Lester group, a prolonged attempt was made to utilize this Wet-TEFM for imaging nicotinic acetylcholine receptors on living cells. However, the complexities of the tip-sample interaction with living cells, combined with the complexities of tip-evanescent field interactions in extracellular liquid, precluded confident interpretation of the resulting data. As a result I was not able to apply this instrument to study

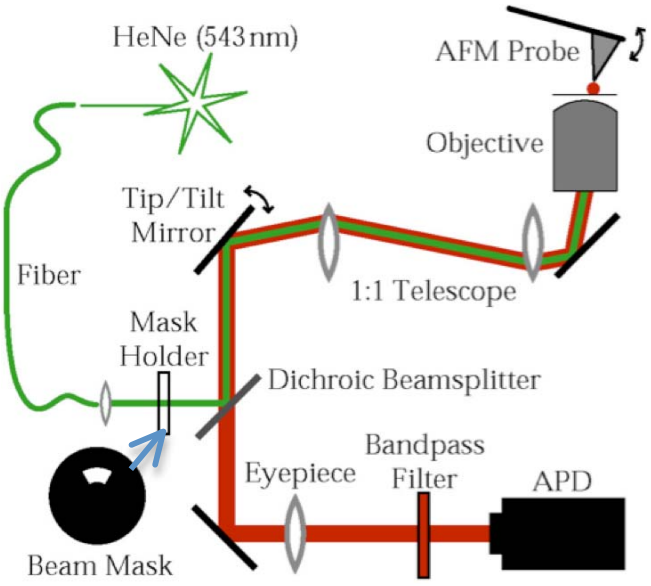


Figure 3.1 The major components in a TEFM are schematically shown above. In essence the TEFM is comprised of an AFM and a TIRF microscope.

neuroreceptor organization and composition as intended.

This chapter is organized into two sections. In the first section 'Dry TEFM Imaging' two papers are presented that describe the TEFM principles, instrument and our results in detail. In the second section 'Wet TEFM Imaging of Live Cells and Membrane-bound Proteins' the innovations developed to enable adaptation of TEFM to imaging live cells are summarized, and some preliminary results are presented. Detailed descriptions of the instrument, data acquisition hardware and software and the image processing software developed for wet TEFM imaging, are presented in Appendix E.

### 3.1 Dry TEFM Imaging

TEFM is a hybrid microscope that combines an Atomic Force Microscope (AFM) with a custom epi-fluorescence optical microscope as shown in Figure 3.2. The excitation laser beam is focused at the top surface of a glass coverslip and emitted fluorescence is directed onto an avalanche photodiode (APD) through a system of spectral filters. Controlled by independent digital feedback loops, the excitation laser focus spot tracks the lateral motion of the AFM probe with a tip/tilt servo mirror.

The TEFM concept couples an AFM probe to a vertically polarized excitation laser, giving substantial enhancement of the optical field strength in analogy with a lightning rod.[3,4,5] The probe apex electric field intensity is enhanced through a geometric lightning-rod effect: resulting in an increase in the fluorescence of samples being imaged by up to 25x (quantum dots). In the context of near-field microscopy, field enhancement near the tip of a sharp probe has been used to generate optical contrast via elastic light scattering,[6,7] Raman scattering,[8] two-photon fluorescence,[4] single-photon fluorescence[9,10,11], and optical second-harmonic generation.[12] The promise of

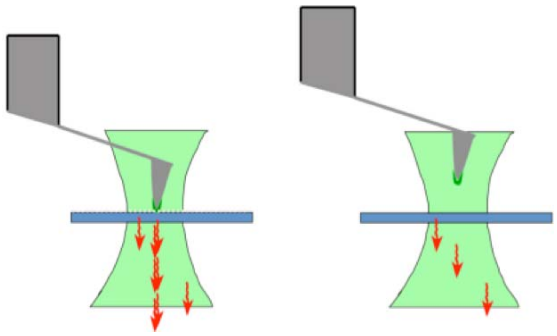

Figure 3.2 Emission is stimulated when the AFM probe tip is proximate to a fluorescent sample. When separated by from the sample by >10 nanometers (left) only the excitation laser stimulated emission can be detected.

these “apertureless” techniques is that spatial resolution is limited only by the sharpness of the tip, overcoming limits imposed by the optical skin-depth in more conventional “aperture” techniques. We reported the first rigorous measurements of the magnitude and spatial extent of the enhanced field near the tip of a silicon atomic force microscope (AFM) probe.[1] The measurements unambiguously confirm an $r^6$ power-law decay whose spatial dependence is moderated by a tip sharpness parameter. Fluorescence from five nm diameter CdSe-ZnS core-shell quantum-dots decay to half their peak value within 1.7 nm of the tip apex. This fluorescence decay-length is several times smaller than previous measurements for either silicon[9] or metal[4,8,11,13]tips.

In air, the silicon AFM probe oscillates above the sample surface with peak-peak amplitude typically between 10 and 40 nm. The tip-enhanced fluorescence signal is superimposed on a significant far-field fluorescence background induced by the diffraction limited excitation laser focus spot.[5] Oscillating the probe with amplitude three or more times the decay length decouples the tip-enhanced field from the background by inducing a strong modulation of the fluorescence photon count rate.[14] Data is recorded in the form of two primary streams: one that marks the arrival time of each detected photon, and one that timestamps the vertical position of the probe. Because the raw data is inherently digital in nature, multiple analysis algorithms can be applied to the data simultaneously without degradation of the signal. By filtering the data at the tapping frequency we suppress the background and generate single-photon fluorescence images of isolated quantum dots with lateral resolution below 10 nm.

References 1 and 2 are included below (J. M. Gerton, L. A. Wade, G. A. Lessard, Z. Ma, and S. R. Quake, Tip-enhanced Fluorescence Microscopy at 10 nanometer Resolution, *Phys. Rev. Lett.*, 2004, *93*, 180801 and Z. Ma, J.M. Gerton, L.A. Wade and S.R Quake, Fluorescence Near-Field Microscopy of DNA at sub-10 nm Resolution, *Phys. Rev. Lett.* **97**, 260801 (2006)) courtesy of the American Physical Society to whom they are copyrighted.

# Tip-Enhanced Fluorescence Microscopy at 10 Nanometer Resolution

Jordan M. Gerton,* Lawrence A. Wade, Guillaume A. Lessard, Z. Ma, and Stephen R. Quake

*Department of Applied Physics, California Institute of Technology, MC 128-95, Pasadena, California 91125, USA*

(Received 12 December 2003; published 28 October 2004)

We demonstrate unambiguously that the field enhancement near the apex of a laser-illuminated silicon tip decays according to a power law that is moderated by a single parameter characterizing the tip sharpness. Oscillating the probe in intermittent contact with a semiconductor nanocrystal strongly modulates the fluorescence excitation rate, providing robust optical contrast and enabling excellent background rejection. Laterally encoded demodulation yields images with $<10$ nm spatial resolution, consistent with independent measurements of tip sharpness.

DOI: 10.1103/PhysRevLett.93.180801 PACS numbers: 07.79.Fc, 42.50.Hz, 61.46.+w, 78.67.Bf

The potential of near-field microscopy to optically resolve structure well below the diffraction limit has excited physicists, chemists, and biologists for almost 20 years. Conventional near-field scanning optical microscopy (NSOM) uses the light forced through a small metal aperture to locally excite or detect an optical response. The spatial resolution in NSOM is limited to 30–50 nm by the penetration depth of light into the metal aperture. More recently, apertureless-NSOM (ANSOM) techniques were developed which leverage the strong enhancement of an externally applied optical field at the apex of a sharp tip for local excitation of the sample [1–11]. The promised advantage of ANSOM is that spatial resolution should be limited only by tip sharpness (typically $\sim$10 nm). The resolution in most previous ANSOM experiments, however, was at best marginally better than NSOM and was inferior to expectations based on tip sharpness alone. Further, the external field used to induce enhancement led to a substantial background signal and to assertions that one-photon fluorescence is not appropriate for ANSOM [12,13]. These experiments fell short of their potential because they maintained a tip-sample gap of several nanometers, and thus did not thoroughly exploit the tightly confined enhancement.

Here, we demonstrate an ANSOM technique that fully exploits the available contrast and leads to spatial resolution that is limited only by tip sharpness. The problems associated with a tip-sample gap are overcome by oscillating the probe in intermittent contact with the sample. The detected signal is then composed of a modulated near-field portion that is superimposed on the far-field background. Subsequent demodulation decouples the two components and thus strongly elevates the near-field signal relative to the background. With this technique, we measured $<10$ nm lateral resolution via one-photon fluorescence imaging of isolated quantum dots, consistent with independent measurements of tip sharpness. The measured resolution is $>3$ times better than previous reports for quantum dots using one-photon fluorescence [8,9], and is $\sim$2 times better than previous measurements using higher-order optical processes (two-photon fluorescence [6], Raman scattering [4,5]) despite predictions to the contrary [12,13].

To better understand the advantages of this technique and to facilitate development of accurate physical models, it is crucial to rigorously characterize the spatial confinement of the enhancement effect. Previous investigations did not attain the level of precision necessary to differentiate between various theoretical models [4,7,14] and there was no experimental or theoretical consensus regarding either the functionality or the set of parameters governing the spatial confinement [12,15–18]. In this Letter, we show unambiguously that the enhancement decays strictly according to a power-law functionality moderated by a single parameter that characterizes the tip sharpness. The collective results shown here will impact not only nano-optics research, but also the application of ANSOM to a wide range of nanoscale systems at the interface between physics, biology, and chemistry.

Our instrument combines a custom optical layout with a commercial (Digital Instruments Bioscope) atomic force microscope (AFM). The excitation laser beam is focused through a glass coverslip (spot size: $350 \times 1000$ nm) using a 1.3 N.A. oil-immersion objective lens. The objective simultaneously collects fluorescence, which is then directed onto an avalanche photodiode through a system of spectral filters (background rejection-ratio $\sim 10^{10} : 1$). A beam-shaping mask is inserted into the excitation beam to generate a purely evanescent field above the glass interface (decay length: 120–250 nm) with a large polarization component along the probe axis [19] as required for field enhancement [15,20]. The focal spot is aligned with the AFM probe by means of a piezoactuated tip-tilt mirror, and the lateral position of the probe is controlled by closed-loop feedback. Uncorrected residual drift (0.05–0.2 nm/s) is the dominant source of uncertainty in the probe position.

The silicon AFM probe oscillates [21] with a typical peak-peak amplitude of 30–40 nm, assuring tip-sample contact at closest approach. In contrast, previous work

  

used very small oscillations (~1 nm) [7,8] or shear-force feedback [4,6,10,14] to maintain a tip-sample gap of several nanometers. Data are recorded to a computer disk in the form of two independent streams of time stamps: one that marks the arrival time of each detected photon, and one that marks a particular phase in each probe-oscillation cycle. Because the raw data are stored permanently in a lossless digital format, multiple analysis algorithms can be applied without degrading the signal.

Samples are prepared by drying a dilute solution of CdSe-ZnS core-shell quantum dots onto a clean glass coverslip. The dots have a mean diameter of ~5 nm and an emission spectrum centered near $\lambda = 600$ nm. The fluorescence rate is highly dynamic, exhibiting "blinking" and sudden changes in quantum yield (QY), in agreement with previous observations [8,22,23]. When a quantum dot is "on" and in a high QY state, a typical count rate of $\sim 2 \times 10^4$ sec$^{-1}$ is measured with ~300 nW of illumination power.

To determine which parameters influence the tip-enhanced intensity distribution we measure the induced fluorescence rate as a function of tip-sample separation ($z$). The focal spot and AFM probe are centered on an isolated dot and the photon and probe-oscillation data streams are recorded for several seconds. A histogram of the phase delay ($\Delta$) between the arrival time of each photon and the preceding probe-oscillation time stamp is computed. Each value of $\Delta$ is then mapped to the corresponding value of $z$ to produce an approach curve (Fig. 1). Each approach curve is a convolution of the tip-enhanced intensity distribution and the excitation-probability distribution within the target. Thus, the fluorescence decays to half its peak value at larger $z$ for increasing target size: 1.7, 4.3, and 6.3 nm for the quantum dot, nanorod, and sphere, respectively. Because of the convolution, the half-maximum at $z = 1.7$ nm for the quantum dot represents an upper limit for the spatial confinement of the tip-enhanced intensity profile. This value is several times smaller than previous measurements for either silicon [7] or metal [4,6,10,14] tips.

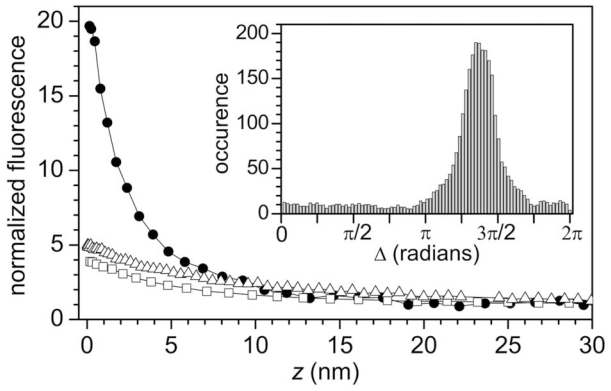


FIG. 1. Enhancement near a sharp silicon probe. Approach curves for a 5 nm diameter quantum dot (solid circles), a 5 × 20 nm CdSe-ZnS nanorod (open squares), and a 20 nm diameter dye-doped latex sphere (open triangles). Additional approach curves extending to $z \sim 150$ nm (not shown) were flat beyond the enhancement region. The vertical scale is normalized to the count rate for a retracted probe. 10% uncertainties in the horizontal and vertical scales originate from calibration of the probe-oscillation amplitude and noise in the normalization factor, respectively. The lines connect the data points. Inset: Histogram of phase delays for the quantum dot.

The fluorescence count rate is enhanced by a factor of 19 for the quantum dot, a factor of 3 for the nanorod, and a factor of 4 for the 20 nm diameter fluorescent sphere. Previous measurements that used silicon tips showed less than a fivefold increase for quantum dots [8,9] and less than a 50% increase for 20 nm spheres [7]. Further, those experiments were complicated by interference effects that yielded a net suppression of the signal relative to the fluorescence background. An additional experiment used a modified aperture-type near-field tip and showed evidence of enhancement that was difficult to quantify [14].

Figure 2 plots each approach curve from Fig. 1 on a log-log scale. Unity is subtracted from the vertical scales of Fig. 1 and the horizontal scales are offset by the fitting parameter $a$, whose physical relevance is discussed below.

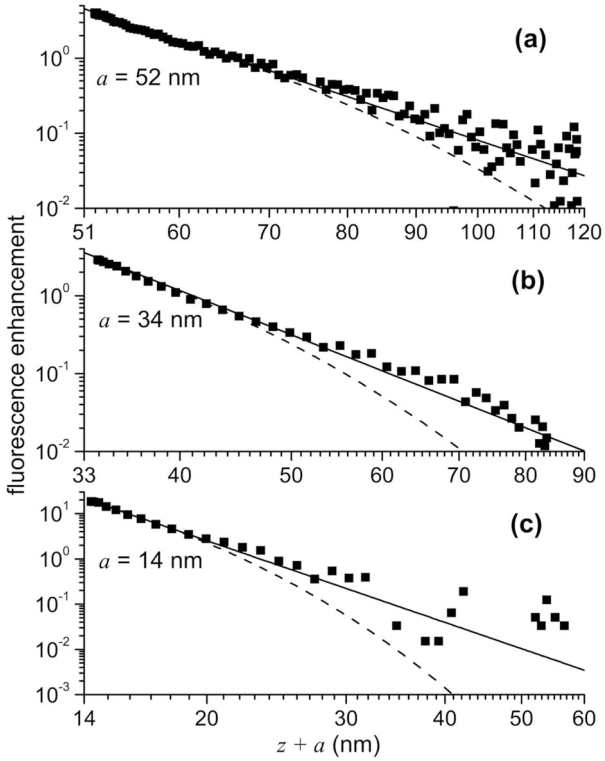


FIG. 2. Least-squares fit to the approach curve for (a) 20 nm diameter dye-doped sphere; (b) nanorod; and (c) spherical quantum dot. Fits to the power law of Eq. (1) (solid curves) and an exponential function (dashed curves) are shown with the data. The horizontal scales are offset by the fitted values of $a$, and unity is subtracted from the vertical scales.

The linear appearance of the data on the log-log scale indicates a power-law decay, and the fluorescence enhancement ($\zeta$) is fit to the function

$$\zeta = \frac{F(z)}{F_\infty} - 1 = \kappa^2 \left( \frac{a}{z+a} \right)^6, \qquad (1)$$

where $F(z)/F_\infty$ is the detected fluorescence rate normalized to the background rate ($F_\infty$), and $\kappa$ is the field-enhancement factor. The solid curves show least-squares fits to Eq. (1) ($\kappa$, $a$ free parameters) while the dashed curves are exponential decays. The data are clearly consistent with a power law, and deviate systematically from the best exponential fit. Previously, both power law [7,14] and exponential [4] decays were fit to experimental data with equal success. The precision of those experiments was insufficient to differentiate between various models because they did not probe the high-contrast region within several nanometers of tip-sample contact.

The measured $(z+a)^{-6}$ decay corresponds to the "near-field" term in the expression for the field intensity near a point dipole, where $z$ is the distance between the apex of the tip and the sample surface. Thus in the limit of an infinitesimally small target particle, the tip-enhanced field is equivalent to a dipole field whose singularity is located within the probe at a distance $a$ from the apex, where $a$ is the tip radius-of-curvature. For finite-sized target particles, the parameter $a$ is a measure of the degree of convolution between the intensity distribution and the excitation-probability distribution, and as expected the fitted values of $a$ increase for larger targets. For smaller targets, $a$ is converging to a value ($\sim$10 nm) that is characteristic of the silicon probes used here. This is evidence that the field decay is indeed moderated only by the sharpness of the tip.

Because this technique utilizes a large probe-oscillation amplitude, the fluorescence rate is modulated with maximum contrast, from the background level when the tip is 30–40 nm above the sample to the peak enhancement at tip-sample contact (Fig. 1). The tip-enhanced intensity profile has no "far-field" component proportional to $r^{-2}$ (Fig. 2) and the corresponding fluorescence profile arises from the "near-field" intensity distribution only. Thus, the depth of fluorescence modulation that results from oscillation of the probe is decoupled from the far-field background and the near-field signal is easily extracted by subsequent demodulation.

A demodulated fluorescence image of a nanorod is shown in Fig. 3(a). The image was generated by raster scanning the AFM probe at a rate of 4 lines/s and then dividing each line into spatiotemporal pixels. These scan rates are at least 5 times faster than previous work for one-photon fluorescence [7–9] and 10 times faster for both two-photon fluorescence [6] and Raman scattering [4]. Pixel values are computed offline as the component of the photon-time-trace's Fourier power spectrum at the probe-oscillation frequency

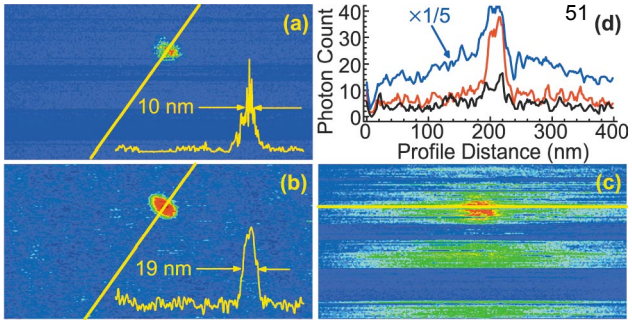


FIG. 3 (color). Tip-enhanced fluorescence image of a nanorod. (a) Fluorescence demodulation signal. (b) AFM probe height (5 nm at peak). (c) Total photon count. Insets in (a) and (b) show signal profiles along the designated axis of length 250 nm. Blue curve in (d) shows the total photon count ( $\times$ 0.2) along the horizontal axis in (c), while red and black curves show the photon count within two ranges of tip-sample separation: $0 < z < 0.4$ nm (red) and $2.5 < z < 4.5$ nm (black). Field-of-view is 400 $\times$ 200 nm: 256 lines of 1024 pixels each.

$$P = \left( \sum_i \sin\Delta_i \right)^2 + \left( \sum_i \cos\Delta_i \right)^2, \qquad (2)$$

where $\Delta_i$ are the measured phase delays and the summation is over all detected photons for the given pixel. When the probe is in the lateral vicinity of the target, the $\Delta_i$ are biased toward the phase value of tip-sample contact where the fluorescence rate is maximally enhanced. Otherwise, the $\Delta_i$ are uniformly distributed and $P$ vanishes to within the shot noise. Comparing Figs. 3(a) and 3(b) shows that the spatial resolution of the demodulated image (see below) is comparable to the tip sharpness and surpasses even the AFM resolution. Comparing Figs. 3(a) and 3(c) demonstrates the effectiveness of the analysis [Eq. (2)] in suppressing the fluorescence background.

Figure 3(d) shows three signal profiles along the horizontal axis indicated in Fig. 3(c) corresponding to the summation of photons over the entire probe-oscillation-cycle (blue), and within a tip-sample separation range of $0 < z < 0.4$ nm (red), and $2.5 < z < 4.5$ nm (black). Here, horizontal profiles are chosen to avoid the regions of quantum-dot blinking [dark stripes in Fig. 3(c)]. As indicated on the figure, the data corresponding to the blue profile have been divided by a factor of 5. Nearly 20% of the detected photons are emitted when the tip apex is within 0.4 nm of the sample surface (red curve) even though this corresponds to only $\sim$3% of the oscillation period. The black curve approximates the typical scanning conditions of previous ANSOM experiments which maintained a tip-sample gap roughly in this range [7–9]. Clearly, those conditions yield both inferior contrast and resolution compared to our technique.

The approach curve measurements (Figs. 1 and 2) suggest a straightforward approach for estimating the

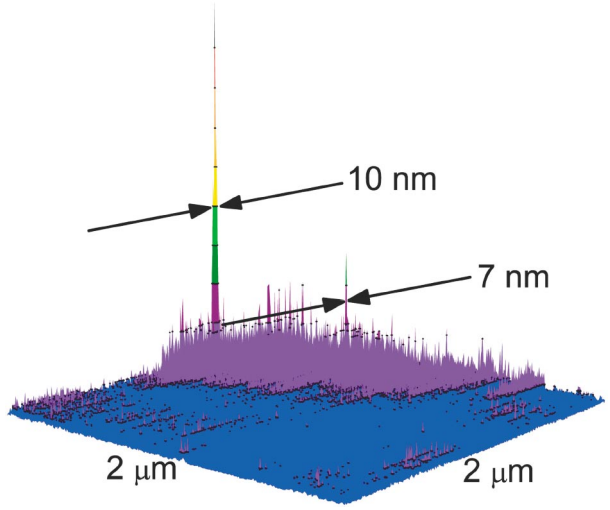


FIG. 4 (color). Tip-enhanced fluorescence image of quantum dots. The degree of contrast is emphasized by false-color relief. The image contains 512 lines of 1000 pixels each. The arrows indicate the measured FWHM for two quantum dots.

spatial resolution. The tip-enhanced field is modeled by a point dipole using a conservative estimate for tip-curvature ($a = 14$ nm) as suggested by the quantum-dot approach curve in Fig. 2(c). A Monte Carlo simulation is then used to generate "mock" data from two hypothetical point sources separated by some distance and the analysis algorithm [Eq. (2)] is applied. The minimum resolvable separation between the point sources is then determined by applying the Sparrow criterion to the demodulated image, i.e., where the central dip between the two sources vanishes [24]. Use of the Sparrow rather than the Rayleigh criterion assures that the estimated resolution is independent of the particular moment calculated in Eq. (2). The simulations suggest a spatial resolution of 11–12 nm for the nanorod images shown in Fig. 3. Figure 4 shows a fluorescence demodulation image of spherical quantum dots in false-color relief. The arrows indicate the measured FWHM for two dots, and the model suggests a spatial resolution of ~8 nm for the smaller one.

In conclusion, we made the first definitive measurement of the tip-enhanced optical field at the apex of a sharp probe and rigorously confirmed a dipolelike model. The technique developed for these measurements overcomes several major obstacles in ANSOM performance and led to the first one-photon fluorescence images with resolution below 10 nm. In contrast to previous work, the tip-enhanced excitation rate is maximized because the probe apex intermittently contacts the sample and thus the enhanced field is probed at atomic-scale distances from the apex. The intermittent tip-sample contact also induces modulation of the excitation rate; demodulating the resultant signal strongly suppresses the problematic far-field background and enables spatial resolution limited only by tip sharpness. The improvements in background suppression and spatial resolution will be even more acute for multiphoton processes (surface-enhanced Raman scattering; coherent anti-Stokes Raman scattering; two-photon fluorescence) compared to one-photon fluorescence, because the induced signal is then more strongly confined at the tip apex. In the future, it may be possible to image samples in a wet environment to measure dynamic processes in molecular-scale structural biology. Finally, it may also be possible to use carbon single-wall nanotubes attached to AFM probes [25,26] to further improve spatial resolution.

We thank Delia Milliron, Ben Boussert, and Paul Alivisatos for the nanocrystals and acknowledge the financial support of Bruce Burrows and Pharmagenomix Inc. J. M. G. was partially supported by the Beckman Institute.

*Permanent address: University of UT, Department of Physics, 115 South 1400 East, Salt Lake City, UT 84112.

[1] F. Zenhausern, Y. Martin, and H. K. Wickramasinghe, Science **269**, 1083 (1995).
[2] H. F. Hamann, A. Gallagher, and D. J. Nesbitt, Appl. Phys. Lett. **73**, 1469 (1998).
[3] R. Hillenbrand and F. Keilmann, Appl. Phys. Lett. **80**, 25 (2002).
[4] A. Hartschuh *et al.*, Phys. Rev. Lett. **90**, 095503 (2003).
[5] T. Ichimura *et al.*, Phys. Rev. Lett. **92**, 220801 (2004).
[6] E. J. Sánchez, L. Novotny, and X. Sunney Xie, Phys. Rev. Lett. **82**, 4014 (1999).
[7] H. F. Hamann *et al.*, J. Chem. Phys. **114**, 8596 (2001).
[8] V. V. Protasenko *et al.*, Opt. Commun. **210**, 11 (2002).
[9] V. V. Protasenko, A. Gallagher, and D. J. Nesbitt, Opt. Commun. **233**, 45 (2004).
[10] A. Kramer *et al.*, Appl. Phys. Lett. **80**, 1652 (2002).
[11] A. Bouhelier *et al.*, Phys. Rev. Lett. **90**, 013903 (2003).
[12] Y. Kawata, C. Xu, and W. Denk, J. Appl. Phys. **85**, 1294 (1999).
[13] L. Novotny, J. Am. Ceram. Soc. **85**, 1057 (2002).
[14] H. G. Frey *et al.*, Appl. Phys. Lett. **81**, 5030 (2002).
[15] L. Novotny, R. X. Bian, and X. S. Xie, Phys. Rev. Lett. **79**, 645 (1997).
[16] J. Azoulay *et al.*, Europhys. Lett. **51**, 374 (2000).
[17] J. L. Bohn, D. J. Nesbitt, and A. Gallagher, J. Opt. Soc. Am. A **18**, 2998 (2001).
[18] Y. C. Martin, H. F. Hamann, and H. K. Wickramasinghe, J. Appl. Phys. **89**, 5774 (2001).
[19] B. Sick *et al.*, J. Microsc. **202**, 365 (2001).
[20] L. Aigouy *et al.*, Opt. Lett. **24**, 187 (1999).
[21] We used NanoDevices Multi75 (50-80 kHz oscillation frequency) and TAP300 (250-350 kHz) cantilevers.
[22] R. G. Neuhauser *et al.*, Phys. Rev. Lett. **85**, 3301 (2000).
[23] M. Kuno *et al.*, J. Chem. Phys. **112**, 3117 (2000).
[24] E. Hecht, *Optics* (Addison-Wesley, Reading, 1990), 2nd ed.
[25] J. H. Hafner *et al.*, J. Phys. Chem. B **105**, 743 (2001).
[26] L. A. Wade *et al.*, Nano Lett. **4**, 725 (2004).

# Fluorescence Near-Field Microscopy of DNA at Sub-10 nm Resolution

Ziyang Ma,* Jordan M. Gerton,† Lawrence A. Wade, and Stephen R. Quake*

*Applied Physics and Physics, California Institute of Technology, Pasadena, California 91125, USA*

(Received 21 October 2005; published 27 December 2006)

We demonstrate apertureless near-field microscopy of single molecules at sub-10 nm resolution. With a novel phase filter, near-field images of single organic fluorophores were obtained with ~sixfold improvement in the signal-to-noise ratio. The improvement allowed pairs of molecules separated by ~15 nm to be reliably and repeatedly resolved, thus demonstrating the first true Rayleigh resolution test for near-field images of single molecules. The potential of this technique for biological applications was demonstrated with an experiment that measured the helical rise of *A*-form DNA.

DOI: 10.1103/PhysRevLett.97.260801 PACS numbers: 07.79.Fc, 42.50.Hz, 87.15.−v, 87.64.Xx

For nano- and molecular science and technology, near-field optical microscopy provides a technique to measure and manipulate structures at subdiffraction limited resolution. The use of a sharp apertureless tip to locally perturb the fields at the sample with apertureless near-field scanning optical microscopy (ANSOM) has allowed spatial resolution at or surpassing 20 nm using elastic scattering [1,2], Raman scattering [3,4], and fluorescence excitation [5,6]. With fluorescence ANSOM, fluorescence of the sample is modified by the proximity of the tip that enhances the excitation field near it, but at the same time induces nonradiative energy transfer (fluorescence quenching) [7]. As a result of the two competitive effects, only single folds of fluorescence enhancement [8–14] or small fractions of fluorescence quenching [15,16] can be measured. Detection of the small high-resolution signal against the classical signal excited by the laser illumination has remained the main concern of fluorescence ANSOM.

Single molecules are widely used as fluorescent tags or reporters in biology [17], sensitive probes in materials and physical chemistry [18], and model single quantum systems for studying light-matter interactions [18]. Near-field optical imaging of single molecules has intrigued scientists since the demonstration by Betzig *et al.* [19]. Unfortunately, it has been a challenge [7,16] to image fluorescent molecules with ANSOM due to the inherent molecular fluorescence fluctuation [inset of Fig. 1(b)] and the limited number of photons available before photochemical destruction (photobleaching) of the molecule. Only two experiments have achieved resolution at 30–40 nm by imaging isolated molecules in vacuum or in a matrix [11] or using a nanofabricated metal tip on top of a fiber aperture [20]. More recently, it was demonstrated that properly designed ''nanoantennas'' can enhance the power of the optical near field by several orders [21,22] or reduce nonradiative energy transfer [23], thus holding promise for imaging single molecules. In this Letter, we demonstrate single-molecule ANSOM imaging at sub-10 nm resolution using a novel phase filter. For the first time, two molecules separated by less than 15 nm can be resolved with ANSOM. We applied this technique to measure the helical rise of *A*-form DNA. The progress we present will accelerate the application of fluorescence ANSOM in the life sciences.

The microscope setup was described previously [6]. Briefly, an atomic force microscope (tapping mode: ~80 kHz) is combined with an inverted confocal optical microscope, with the silicon tip (FESP, Veeco Instruments) aligned with the laser focal spot [Fig. 1(a)]; the fluorescence photons and the beginning of the tip oscillation cycles were recorded as time stamps.

We imaged isolated Cy3 molecules and Cy3 molecule pairs. Each Cy3 molecule is attached to the 5′ end of a

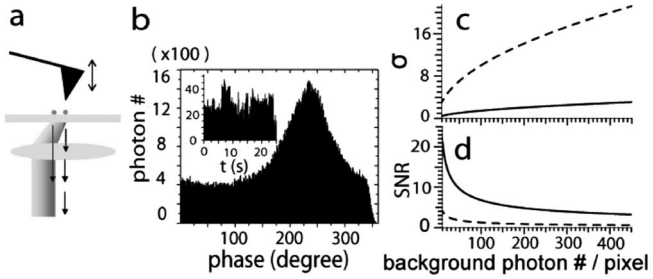


FIG. 1. (a) Illustration of the microscope. The linearly polarized beam, passing through a mask with a wedged window (not shown), is at total internal reflection at the substrate-air interface (focus area ~350 × 1000 nm) to achieve a large field component along the tip axis. (b) Tip-oscillation phase histogram of the photons. The inset is a typical fluorescence time trace of a Cy3 molecule, where the vertical axis is the photon count per 0.01 s. (c) The background noise (standard deviation) obtained from the phase filter (solid curve) and from the unfiltered shot noise, $\sqrt{n}$ (dash curve). The horizontal axis is the same as (d). (d) The SNR calculated as the image pixel signal divided by the background noise from the phase filter (solid curve) and from the unfiltered shot noise (dash curve). The image pixel signal is $0.60fN/3$ ($f$: fluorescence enhancement; $N$: photon number per pixel emitted by a typical molecule) for the solid curve according to Eq. (1), and $0.75fN/3$, which is the direct sum of the near-field photons [Fig. 1(b)], for the dash curve. For both curves, we used $f = 5$, $N = 10$.

 

60-mer single-stranded DNA (ssDNA). Each pair of Cy3 molecules is linked by a 60 bp double-stranded DNA (dsDNA), prepared by annealing two complementary 5′-labeled ssDNA. The dsDNA chain is shorter than the DNA persistence length (~150 bp), so it is rigid. To obtain topographical atomic force microscope (AFM) images of the DNA molecules, we used glass–mica hybrid slides [24]. To prepare the samples, 1 $\mu$l of 10 nM DNA solution was spread on the mica surface and evaporated dry, then the surface was rinsed with deionized water and dried with nitrogen gas. The majority of the molecules on the surface produced more than $10^5$ photon counts, allowing >20 s imaging time.

The signal of fluorescence ANSOM contains the near-field and far-field components excited by the optical near-field and propagating laser illumination, respectively. With single molecules, fluorescence enhancement is only ~twofold to fivefold [Fig. 1(b)], comparable to the fluctuation of the far-field signal [inset of Fig. 1(b)]. In previous work [6], we demonstrated that signal demodulation separates the far-field and near-field signals successfully. This method, however, requires a large number of photons and works only for intense targets, such as quantum dots (Fig. 4 of Ref. [6]). To find an efficient separation method, we studied the $2 \times 10^5$ fluorescence photons from an isolated Cy3 molecule probed by an oscillating tip. Figure 1(b) is the tip-oscillation phase histogram of the photons, from which phase $\phi_0$ for the maximum fluorescence enhancement can be determined. It was found from experiments that $\phi_0$ remains the same with the same type of tip, and the profile of fluorescence enhancement can be approximated by

$$g[\phi - \phi_0] = \exp\left(-\frac{|\phi - \phi_0|_p^2}{60^2}\right) \qquad (0 \le \phi, \phi_0 < 360)$$

where $|\phi - \phi_0|_p$ is defined as $\min(|\phi - \phi_0|, |360 - |\phi - \phi_0||)$. We calculated the raw near-field signal $S_{\mathrm{rn}}$ of a pixel as

$$S_{rn} = \sum_{|\phi-\phi_0|_p \le 60} \exp\left(-\frac{|\phi - \phi_0|_p^2}{60^2}\right) D[\phi], \qquad (1)$$

where $D[\phi]$ is the number of photons at phase $\phi$. This formula is a bandpass phase filter that passes photons within 60 deg of $\phi_0$ [Fig. 1(b)] with weights determined from $g$. The width of the bandpass window was optimized to increase the passed photons and to reduce the bleed-through between the near-field and far-field signals. The far-field signal $S_f$ was calculated as

$$S_f = \sum_{|\phi-(\phi_0-180)|_p \le 60} \exp\left(-\frac{|\phi - (\phi_0 - 180)|_p^2}{60^2}\right) D[\phi] \qquad (2)$$

such that molecules outside the near-field volume of the tip contribute equally to $S_{\mathrm{rn}}$ and $S_f$. $S_f$ was then averaged with those of its four neighboring pixels to get $\bar{S}_f$. The[54] pixel signal was calculated as $S_n = S_{\mathrm{rn}} - \bar{S}_f$ for $S_{\mathrm{rn}} > \bar{S}_f$ and $S_n = 0$ for $S_{\mathrm{rn}} < \bar{S}_f$.

The phase filter effectively suppresses the noise of the background, where we refer to the background as an area without near-field images. One can estimate the effect of the filter by approximating $g$ with a top hat function, with which we can calculate the mean and variance of the background as $\tilde{x} = \sum_{i=0}^{\infty}\sum_{j=0}^{\infty} jP(5i, 5n/3) \times P(i + j, n/3)$ and $\tilde{\sigma}^2 = \sum_{i=0}^{\infty} P(5i, 5n/3)\{\sum_{j=0}^{\infty}(j - \tilde{x})^2 P(i + j, n/3) + \sum_{j=0}^{i} \tilde{x}^2 P(j, n/3)\}$, respectively, where $i$ and $j$ are dummy variables, $n$ is the average photon number per pixel in the background, and $P(a, b) = (e^{-b}b^a)/a!$ is the Poisson probability density. The effect of using a Gaussian for $g$ causes only a small change in the standard deviation of the background, giving $\sigma = 0.75\tilde{\sigma}$. Compared with the unfiltered shot noise, the background noise is effectively suppressed with the phase filter [Fig. 1(c)], which provides ~sixfold improvement in the signal-to-noise ratio (SNR) and makes it possible to image multiple fluorescent targets in the focal spot [Fig. 1(d)]. Assuming that a far-field illuminated molecule emits 10 photons per pixel, good SNR (>7) can be obtained with up to ten molecules in the focal spot and fair SNR (>3) with several tens of molecules in the focal spot [Fig. 1(d)]. The SNR obtained in experiments (Figs. 2 and 4), determined as the difference between the peak image signal and the background baseline divided by the variation of a 100 × 100 nm background area, is in good agreement with the calculation [Fig. 1(d)].

We imaged 211 isolated single Cy3 molecules. The images are either symmetric [Fig. 2(a)] or elongated [Fig. 2(b)], due to different molecular dipole orientations

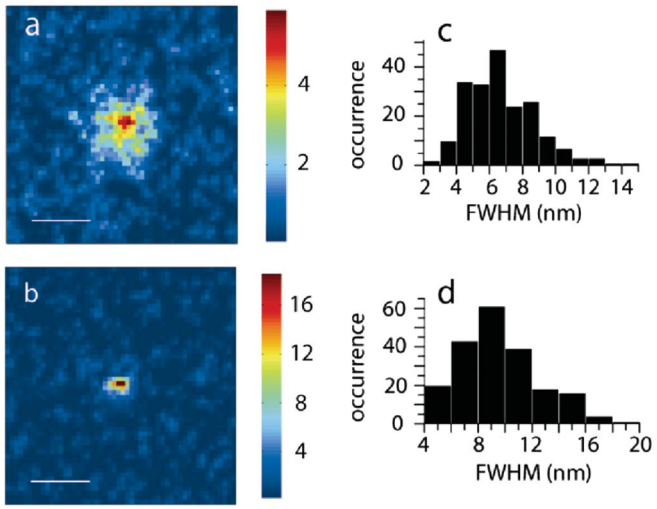


FIG. 2 (color). (a), (b) Near-field images of isolated Cy3 molecules. Each figure was extracted from a 1 × 1 $\mu$m, 512 × 512 pixel image. The SNR for (a) and (b) is 16.2 and 25.5, respectively. Scale bars: 25 nm. (c), (d) Histograms of FWHM measured along the minor and major directions, respectively.

(discussed below). Histograms of full width at half maximum (FWHM) measured along the minor and major directions of the 211 images are shown in Figs. 2(c) and 2(d), with the average at 6.8 and 9.6 nm, respectively. It is clear that simply choosing the linewidth of a single image is not an accurate method for determining resolution, for the images are highly variable. Here we define an average resolution of 8.2 nm, which is ~3–4 times better than the previous best ANSOM measurements and close to 1 order better than typical results of apertured near-field microscopy.

To better understand the results, we simulated images of single molecules using the electrostatic dipole model of the tip. This model was adopted in both fluorescence ANSOM and scattering ANSOM [1,25] and was supported by numerical simulations [26]. According to the model, the total field amplitude is

$$\vec{E}(\vec{r}) = E_0\left[\hat{z} + \alpha\left(\frac{3z}{r^4}\hat{r} - \frac{1}{r^3}\hat{z}\right)\right], \quad (3)$$

where $E_0$ is the external laser field, $\alpha$ is determined experimentally and the coordinate origin is at the tip center. Using $[E(r) \cdot p(\theta, \varphi)]^2$ as the image intensity, simulation results [Fig. 3(a)] show that as $\vec{p}$ tilts away from the tip axis, the image becomes elongated and the image center shifts away from the molecule; when $\vec{p}$ is perpendicular to the tip axis ($|\theta - 90°| \leq 0.8°$), the image has two symmetric "lobes"; when $\theta$ is close to 90° ($0.8° \leq |\theta - 90°| \leq 20°$), there is a small region where the signal is below the background. For nonzero $\varphi$, the images are simply $\varphi$-degree rotation of those for $\varphi = 0$ [Fig. 3(a)], for the field is symmetric about the tip axis. Simulation patterns for $\theta$ at or close to 90° were experimentally observed [Figs. 3(b)–3(d)], providing direct support for the electrostatic dipole model.

Measuring true resolution has long been a challenge in near-field microscopy; one of the strongest tests is to make a "Rayleigh" resolution measurement, in which two proximate point sources are resolved. To our knowledge there have been no rigorous near-field measurements such as this made with single molecules, which are excellent approximations of a point source. With the phase filter, we were able to resolve two Cy3 molecules linked by a 60 bp dsDNA oligonucleotide. Figures 4(a)–4(c) are the near-field optical images of such molecule pairs, where Figs. 4(d)–4(f) are the corresponding topographical AFM images. ANSOM has a better resolution than AFM even with the same tip, because the force involved in AFM, which is proportional to the inverse of the tip-sample distance [27], decays much more slowly than the optical near field. There are no previous AFM experiments that resolved DNA molecules as short as 15 nm; instead, round images for short DNA molecules were observed in this [Fig. 4(d)] and previous experiments [28].

We imaged a total of 389 dsDNA oligonucleotides, 29% of which showed resolvable Cy3 pairs. The Cy3 labeling efficiency for each DNA strand is about 80%, so we expect that 67% of the optically detectable DNA oligonucleotides are actually labeled with two Cy3 molecules. Factors such as imperfect annealing, photobleaching, and worn tips can all contribute to the failure to resolve the rest. As a control experiment, the 211 images of single Cy3 molecules were analyzed in the same fashion and double-lobed artifacts were found in only 4% of the images [Fig. 4(h)], which is a

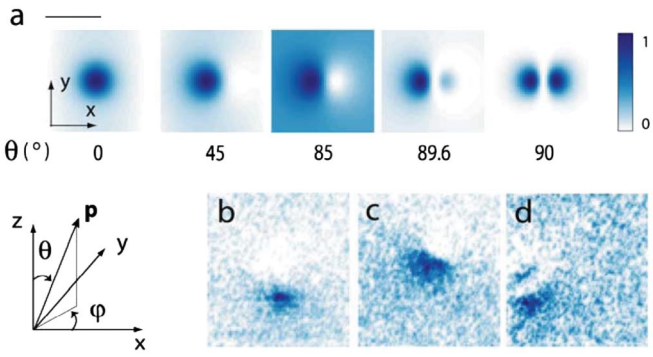


FIG. 3 (color). (a) Simulated images with the tip radius at 10 nm and fluorescence enhancement at 5. Scale bar: 20 nm. (b)–(d) Experimental images (150 × 150 nm) showing the same patterns as the simulated ones. In these images, $S_{rn}$ was used as the pixel signal.

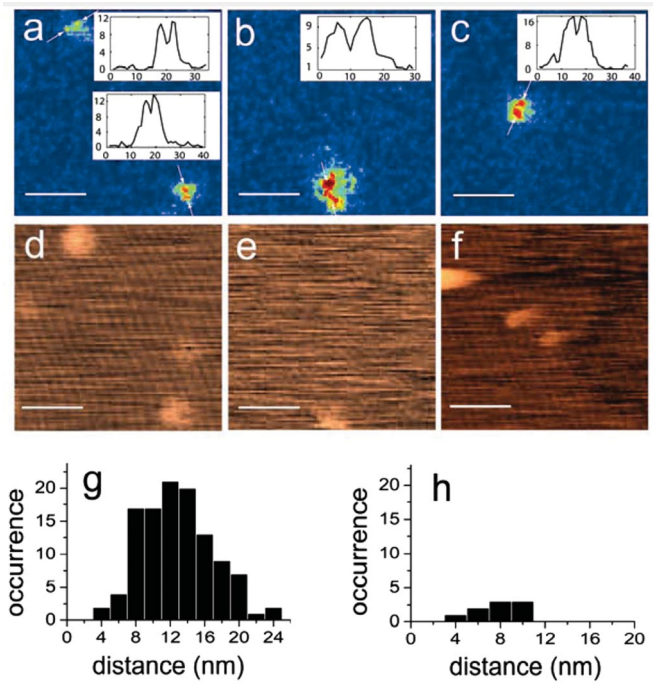


FIG. 4 (color). (a)–(c) Near-field images of Cy3 pairs. The SNR is 12.4 and 15.9 for (a), 16.1 for (b), and 20.4 for (c). The insets show the profiles with line cut through the image centers (indicated by arrows), where the horizontal axis is in pixels (1 pixel = 1.95 nm) and the vertical axis is the pixel signal. (d)–(f) AFM images corresponding to images (a)–(c), respectively. Scale bars: 50 nm. (g) Histogram of distances between the resolved Cy3 molecules. (h) Histogram of distances between the two artifactual lobes of single Cy3 molecules.

vast improvement over a previous method which has artifacts in all images [20].

With the resolved Cy3 molecule pairs, the end-to-end distances of the 60 bp DNA oligonucleotides can be measured [Fig. 4(g)]. The statistical result is 13.0 nm ± 4.1 nm (standard deviation) with standard error of the mean $\sigma_\mu = 0.4$ nm. Random factors that contribute to the distribution of the measurements include limited precision in determining the image centers, shifting of the images, and the flexible carbon linker (~0.6 nm) between the Cy3 molecule and DNA. Systematic errors also exist in the result. Simulation shows that the two images shift toward each other because the tip enhances both molecules when it is in between them; the shift increases with larger tip radius. The linewidth of the majority of the images indicates an upbound of the tip radius at 15 nm, at which a 2.5 nm shift was simulated for two molecules separated by 15 nm. Therefore, the precision of our measurement of the DNA length has a statistical error of 3% and a systematic error up to 20%.

DNA structure depends strongly on humidity and takes the *A*-form and *B*-form structure at low and high humidity, respectively. It is now understood that DNA-binding drugs and proteins can induce local conformational conversion between the two forms [29]. In our experiments, the DNA molecules were imaged at humidity (~30%) well below the 73% threshold for the *A*-form DNA. An unresolved paradox in x-ray diffraction studies of *A*-form DNA is that fibers of long DNA molecules with mixed sequences yield a consistent value of 2.6 Å/bp for the helical rise [30], but crystal structures of small oligonucleotides (~10 bp) reveal an average value of 2.83 Å/bp with a standard deviation of ~0.36 Å/bp across different sequences [31]. The source of the discrepancy is as yet unresolved, although crystal artifacts, molecular weight effects, and incomplete sequence sampling may all play a role. Our measurements described above allow an independent determination of the helical rise, and do not suffer from artifacts due to crystal packing or small molecular weights. The result (2.17 Å/bp) agrees with the x-ray data of fibers within one sigma of our largest estimated experimental error and falls within the two sigma limit of the sequence-dependent variation observed in crystal structure data.

The phase filtering method should be applicable to nanoantennas [21–23] and supersharp carbon nanotube probes [32] with which both the resolution and the precision can be improved. With the advances of AFM technology, such as imaging in water and fast frame imaging speeds, it may ultimately be possible to combine optical resolution approaching that of electron microscopy with the ability to image biomolecules in physiological conditions.

The authors thank G. Lessard for contributions to the development of initial data acquisition and data analysis algorithms. This work was supported by Pharmagenomix Inc. and the NIH Director's Pioneer program.

*Present Address: Dept. of Bioengineering, Stanford University and Howard Hughes Medical Institute, Stanford, CA 94305, USA.

†Present Address: University of Utah, Dept. of Physics, 115 South 1400 East, Salt Lake City, UT 84112.

[1] F. Zenhausern, Y. Martin, and H. K. Wickramasinghe, Science **269**, 1083 (1995).
[2] R. Hillenbrand and F. Keilmann, Appl. Phys. Lett. **80**, 25 (2002).
[3] A. Hartschuh *et al.*, Phys. Rev. Lett. **90**, 095503 (2003).
[4] T. Ichimura *et al.*, Phys. Rev. Lett. **92**, 220801 (2004).
[5] E. J. Sánchez, L. Novotny, and X. S. Xie, Phys. Rev. Lett. **82**, 4014 (1999).
[6] J. M. Gerton *et al.*, Phys. Rev. Lett. **93**, 180801 (2004).
[7] J. Azoulay *et al.*, Europhys. Lett. **51**, 374 (2000).
[8] H. F. Hamann, A. Gallagher, and D. J. Nesbitt, Appl. Phys. Lett. **76**, 1953 (2000); H. F. Hamann *et al.*, J. Chem. Phys. **114**, 8596 (2001).
[9] V. V. Protasenko *et al.*, Opt. Commun. **210**, 11 (2002).
[10] V. V. Protasenko, A. Gallagher, and D. J. Nesbitt, Opt. Commun. **233**, 45 (2004).
[11] V. V. Protasenko and A. C. Gallagher, Nano Lett. **4**, 1329 (2004).
[12] J. Azoulay *et al.*, J. Microsc. **194**, 486 (1999).
[13] N. Hayazawa, I. Inouye, and S. Kawata, J. Microsc. **194**, 472 (1999).
[14] A. Kramer *et al.*, Appl. Phys. Lett. **80**, 1652 (2002).
[15] T. J. Yang, G. A. Lessard, and S. R. Quake, Appl. Phys. Lett. **76**, 378 (2000).
[16] W. Trabesinger *et al.*, J. Microsc. **209**, 249 (2003); W. Trabesinger *et al.*, Appl. Phys. Lett. **81**, 2118 (2002).
[17] S. Weiss, Science **283**, 1676 (1999).
[18] W. E. Moerner and M. Orrit, Science **283**, 1670 (1999).
[19] E. Betzig and R. J. Chichester, Science **262**, 1422 (1993).
[20] H. G. Frey *et al.*, Phys. Rev. Lett. **93**, 200801 (2004).
[21] P. J. Schuck *et al.*, Phys. Rev. Lett. **94**, 017402 (2005).
[22] P. Mühlschlegel *et al.*, Science **308**, 1607 (2005).
[23] J. N. Farahani *et al.*, Phys. Rev. Lett. **95**, 017402 (2005).
[24] A thin layer (~2 $\mu$m) of mica was lifted off a mica sheet and placed on a clean glass cover slide; bonding between the two surfaces is immediate, probably due to van der Waals forces. The mica surface was treated with 20 mM $MgCl_2$ and rinsed by deionized water.
[25] B. Knolland and F. Keilmann, Nature (London) **399**, 134 (1999).
[26] A. Bouhelier *et al.*, Phys. Rev. Lett. **90**, 013903 (2003).
[27] F. J. Giessibl, Rev. Mod. Phys. **75**, 949 (2003).
[28] H. G. Hansma, Nucleic Acids Res. **24**, 713 (1996).
[29] X.-J. Lu, Z. Shakked, and W. K. Olson, J. Mol. Biol. **300**, 819 (2000).
[30] S. B. Zimmerman, Annu. Rev. Biochem. **51**, 395 (1982).
[31] X.-J. Lu and W. K. Olson, Nucleic Acids Res. **31**, 5108 (2003).
[32] J. H. Hafner *et al.*, J. Phys. Chem. B **105**, 743 (2001); L. A. Wade *et al.*, Nano Lett. **4**, 725 (2004).

## 3.2 Wet TEFM Imaging of Live Cells and Membrane-bound Proteins

The basic concepts that enable wet TEFM imaging are very similar to those upon which the dry TEFM microscope was built. Wet TEFM also relies on the modulation of fluorescence when the tip is proximate to a fluorophore. As with the original microscope the wet imaging TEFM also combined a homebuilt TIRF optical microscope with an atomic force microscope.[15] Detailed pictures of the wet TEFM instrument and filter specifics are presented in Appendix E. The data acquisition system specification and design is also included in Appendix E along with the complete image processing code developed for this project.

TEFM imaging of live cells is substantially more difficult than imaging hard, dry samples on atomically smooth surfaces. To a large extent this is true because this technique fundamentally relies on tip stimulated, and modulated, fluorescence. Achieving near-field, tip stimulated fluorescence essentially requires that the AFM probe contact the sample fluorescent labels. It also requires that the AFM probe be oscillated, so that tip-sample contact is periodic, to enable modulation of the sample fluorescence.

In AFM terms, probe oscillation with periodic contact is referred to as 'tapping mode' operation. Unfortunately wet tapping mode imaging of living cells is very, very difficult. Instead of tapping mode, contact mode, in which the tip remains in constant contact with the sample being imaged, is used by the AFM community for imaging biological samples. Also, there were no prior studies, theoretical or experimental, of tip-enhanced fluorescence in a liquid environment.

This discussion is focused on those issues that are specific and unique to wet-sample TEFM imaging. As a result of these challenges, many innovations were developed to enable the capability to image live cells. Some of these challenges, and the solutions that solved them, are described below.

**The objects being observed (cells) are large compared with the ~7 micron Field-of-View (FoV) our microscope was capable of.**

In the dry TEFM, the sample was kept still as the laser and AFM probe were synchronously rastered over it. The FoV of the microscope described in our PRL publications was limited by the range of the tip-tilt mirror that directed the excitation laser such that it stayed focused on the tip of the AFM probe as it was rastered over the sample. Therefore a new mode of operation, sample scanning, was introduced. To accomplish this an nPoint piezoelectric X-Y sample scanning stage with a 100 micron range[16] was installed. The data acquisition and control software and image processing software were also modified to enable operation in this new mode. With the sample stage in place the laser focal spot was focused onto the AFM probe tip. The laser and AFM probe were then held stationary in X-Y while the sample was rastered. With this change the largest area that could be scanned was increased from ~49 square microns to ~10,000 square microns. This is large enough to fully capture one or more N2a cells.

To image a sequence of cells within a given culture dish the nPoint sample stage was mounted to a second, long-range X-Y translation stage. This long-range X-Y translation stage is driven with two manual 100-pitch thumbscrews. These move the nPoint sample stage approximately 125 microns with one half-turn.

**The microscope objective used in our previous work was incompatible with doing TIRF with water above the coverslip.**

Total internal reflection fluorescence microscopy, as implemented in our TEFM, relies on an excitation laser the exits the microscope objective at such an extreme angle that it reflects at the glass coverslip-sample interface rather than transmitting. The reflected light, being electromagnetic radiation, induces an evanescent field on the sample side of this interface. It is this evanescent field that we use for exciting fluorescence in the sample.

The maximum angle at which a collimated laser beam can leave an objective is described by the objective's Numerical Aperture (NA). The higher the NA value, the greater the maximum angle is for a given transmitting media.

The infinity corrected microscope objective used for all of our dry sample TEFM imaging was only a 1.3 NA oil immersion objective.[17] Since water has an index of refraction of 1.33 this objective would not be used to do objective-based TIRF of a wet sample. A 1.45 NA oil immersion microscope objective[18] was procured that was compatible with wet sample TIRF.

An unusual feature of this TIRFM was that the excitation laser entered the back aperture as a collimated beam and so was focused at the coverslip surface. As a result, the sample was not illuminated by the laser until the image was actually being acquired. This helped to reduce photobleaching of the sample. In contrast, most objective-based TIRFMs, including the one described in Chapter 2 of this thesis, are designed so that the excitation laser is focused on the objective back aperture and so achieve a uniform illumination over a large area at the cost of additional photobleaching of the sample.

**Normal AFM probe holders are capable of tapping mode oscillation are not compatible with imaging in water.**

The normal tapping mode AFM tip holder is designed to work on dry samples. Among other issues it has exposed electrical connections to power the tiny piezo chip that drives the high frequency oscillation in z. An alternate method for driving tip oscillation in liquid is called z-demodulation. In that mode the entire piezo column is oscillated. The probe holder acts like a piston that oscillates the entire end of the AFM. Doing so alternately pressurizes and depressurizes the liquid (and cell). The probe tip position oscillates relative to the sample holder because due to interaction with the liquid environment. However I found that this mode of operation significantly distorted live cells. In addition, the Veeco Nanoscope IV AFM control electronics incorporated a low-pass filter in the z-demodulation circuit that was set at 20 kHz. Since silicon AFM

probes that will perform tapping mode in water oscillate at frequencies between 16 and 70 kHz I discovered that the AFM drive circuitry was attenuating it's own drive signal.

To solve this a liquid-compatible probe holder made by Veeco[19] was procured, in which the piezo chip and its electrical connections were encapsulated. This device was intended for tapping mode operation in water. Since the drive signal comes through the tapping mode circuit in the AFM controller rather than the z-demodulation circuit there was no issue with self-attenuation using this holder. The direct drive probe holder is relatively large however and so the AFM stand had to be raised to accommodate it. The size of the tip holder also precluded the use of small cell culture dishes. MatTek manufactures cell culture dishes with a 50 mm diameter, and a large coverslip compatible with this larger AFM probe holder.[20] The glass coverslip was a number 0 thickness, which was compatible with doing TIRF through the new 1.45 NA microscope objective.

**TEFM requires that the AFM probe tip oscillate (tap) in such a manner that the probe alternately makes contact with the sample and then oscillates above the sample. Such 'tapping-mode' AFM imaging is done at a frequency near the resonant frequency of the AFM probe cantilever. In air there is very little damping of this oscillation. However, the viscous nature of water substantially damps the AFM probe oscillation and thereby precludes imaging at the very high frequencies (200-400 kHz) typical. In addition, wet cells and membranes are soft resulting in tip-induced physical deformation of the cells.**

As described in the 'Dry Imaging' section, the TEFM is fundamentally based on combining an AFM with a TIRFM. The advantage of this technique comes from interactions between the AFM probe tip and the TIRF evanescent field. The large electric field resulting from these interactions at the tip of the probe in turn stimulates fluorescence through a non-radiative dipole-dipole near-field interaction. This $1/r^6$ nature of near-field fluorescence stimulation requires that the tip either touch the

fluorophore significant or approach to within a nanometer if near-field fluorescence enhancement is to be observed.

Normal tapping mode AFM probes are designed to oscillate at high frequency in air. Much of the positional uncertainty in this system is due to chaotic oscillation modes. As a result the primarily random noise in any one image-pixel is reduced by the square root of the number of taps within it. As a result: the higher the tapping frequency the faster an image can be made without degrading image quality. The stiffness of a typical silicon AFM probe cantilever ranges between 40 and 50 N/m. A live cell is much softer than such a probe. So commercially available probes that are designed for tapping mode imaging are inappropriate for imaging live cells in liquid.

Therefore a softer cantilever was required if the soft sample was not to be significantly deformed during contact. Most 'soft' cantilever AFM probes are made of silicon nitride, which is an insulator. We found previously that the best tip enhancement occurred with doped-silicon AFM probes and that silicon nitride cantilevers produced no tip enhancement.

After investigating many options it was discovered that silicon force mode AFM probes were capable of tapping mode imaging in water. In particular I found that Nanosensors ATEC-FM and PPP-FMR AFM probes[21] worked reasonably well on firm wet samples although less well on live cells. These silicon AFM probes typically operate at ~30 kHz in water with a cantilever stiffness of 2.8 N/m. No solution was found that enabled high quality tapping mode imaging of live cells using a semi-conductive probe.

**AFM tip alignment with the excitation laser is much more difficult in water as the alignment laser is refracted by the water and its container. In addition, cell covered coverslips are not atomically smooth or essentially free of fluorescent contamination as the dry samples previously imaged were.**

Tip alignment with the focal spot of the excitation laser is critical in tip-enhanced imaging. It was found that the AFM probe can be illuminated in water with a 670 nm

laser diode[22] such that it produces a very clearly defined diffraction pattern (see Figure 3.1 a). If water is just pooled over the sample, refraction of the alignment laser normally precluded alignment. However it was found that the side of a cell culture dish is sufficiently flat that this technique works in water as well as in air. This diffraction pattern can be imaged by the optical microscope objective (see Figure 3.1b-d) when this probe is in contact with, or very close to, the glass surface. By comparing the relative positions of the reference laser spot and the probe diffraction pattern as imaged by the microscope objective it is easy to consistently position the AFM probe within ~$\lambda$/25 (~30 nm) of a defined point.

In some cases the cells on the surface would scatter the alignment laser light so much as to make it hard to differentiate the tip diffraction pattern. In that situation, the laser was initially aimed higher up the AFM such that the beam is bounced off the dichroic directly down onto the cantilever. The shadow of the cantilever can be used to put the tip very close to the excitation laser backscatter. Final tip-laser alignment could then be carried out in the normal manner.

**Most biological experiments based on fluorescence imaging require the detection of at least two fluorophore colors. Such two color imaging often requires excitation at several different laser wavelengths.**

To accomplish this a second TEFM was constructed capable of imaging in two colors and using three fiber-coupled excitation lasers (442 nm, 502 nm and 543 nm). This optical and mechanical configuration of this microscope is shown Appendix E. Another significant difference in this microscope is that it utilizes two methods of producing a p-polarized evanescent field. One is based on the mask technique used previously. The second is based on use of a radial polarization filter.[23] The radially polarized beam that emerges from that filter has several more complicated modes. So the beam is then focused on a pinhole chosen and positioned to transmit only radially polarized light. In this microscope excitation beam alignment is done using a tip-tilt mirror through a 1:1 telescope in a manner similar to the earlier instrument. AFM positioning is done using

X and Y translation stages driven by actuators. The same nPoint sample scanning stage is used along with the same gross positioning X-Y translation stage. All of the filters were custom made by Chroma and suitable for single molecule imaging.[24]

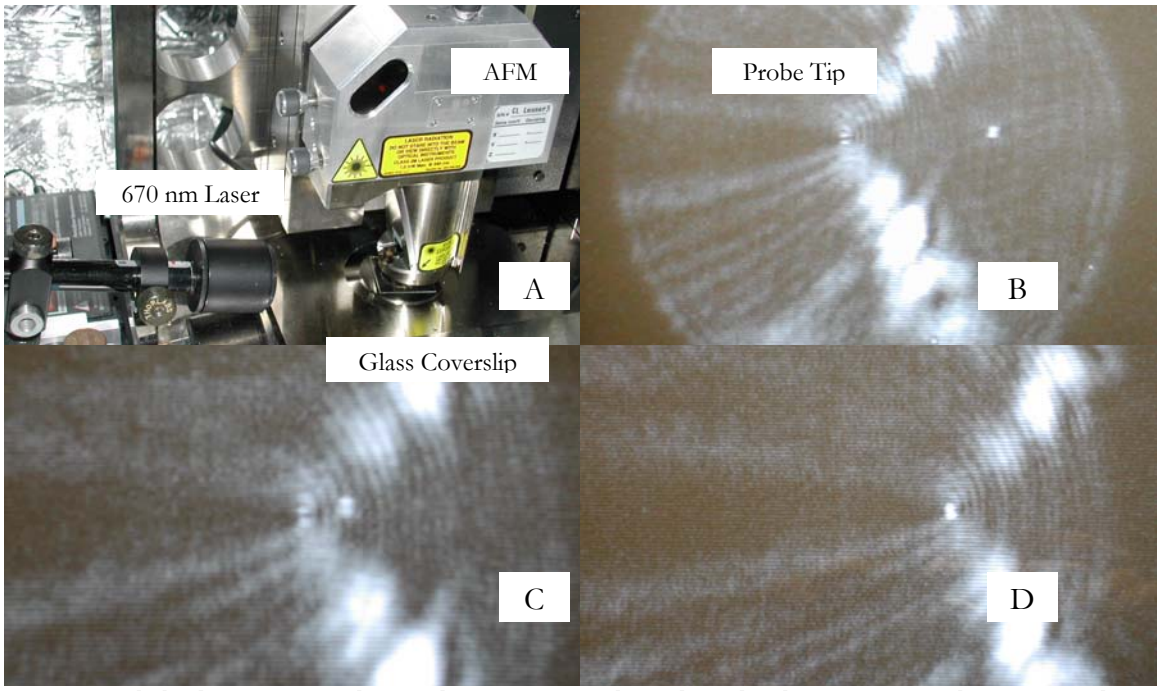


Figure 3.3. A hybrid AFM/Inverted Optical microscope with single molecule sensitivity is shown in panel A. A diffraction pattern is cast by the tip of the AFM probe (panel B) when <50 nm off the coverslip surface under illumination from the laserpointer. The 543 nm reference spot, seen to the left of this pattern, is approximately 9 μm from the probe tip. In panel C, the diffraction pattern is 1.45 μm in X and 450 nm in Y from the reference spot. In panel D the two are aligned.

**Even in optimal conditions, AFM imaging of live cells using tapping mode is problematic due to the forces involved. In addition the evanescent field has a typical penetration depth of 100-200 nm in cells. Cells are thicker than 200 nm. As a result imaging the top of the cell will not result in significant tip enhanced fluorescence emission because the evanescent field will have completely decayed by the top of the cell.**

While required for efficient stimulated emission, contact with the typical, stiff AFM probe tends to deform the cell surface. As mentioned earlier one way to minimize that distortion is to image with soft AFM probes. Another method for minimizing sample

distortion is to not image a live cell. Instead the cell can be adhered to the surface of a cell. Such adhesion can be achieved by growing the cell on an APTES coated coverslip. Extracellular proteins can be covalently attached to such a surface. Alternately, an APTES coated coverslip can be placed on top of cultured cells. The membrane-bound proteins can be made to covalently bond to the coverslip. After attachment, by cytolysis, the cell can be ruptured and the membrane skeletal membrane gently washed off.

The remaining attached membrane ghost can be imaged directly. The membrane ghost, being attached directly to the coverslip, is in the strongest portion of the evanescent field. The fluorescent labeling is best located on the cytosolic side of the cell membrane for this approach. In that fashion the tip can directly approach the fluorescent label. Protocols used to successfully produce such specimens are presented in Appendix B. The protocols included in Appendix B detail APTES coating the coverslip, cell adhesion, hypotonic cell lysis, cell plating and transfection.

In summary, this approach has the advantages of placing the sample within the maximum intensity of the evanescent field, exposing cytosolically labeled proteins directly to the AFM probe, and minimizing mechanical distortion. Imaging membrane ghosts rather than live cells should be the clear choice of preference in any future studies.

**Wet tapping mode imaging can only be done at line scan rates of 3 lines/second or fewer. Typically 1 line per second was used for imaging. A 512 line image therefore typically took 512 seconds to acquire. The large (~1 GB) dataset acquired took 20-40 minutes to transfer and process before an image could be seen. This made it very difficult to scan a culture dish to identify healthy cells. As a result imaging 10 cells took at least 14 hours.**

A method for normal real-time fluorescence imaging was developed and incorporated into the TEFM. A photon counter[25] was used that output a DC voltage directly proportional to the photon flux seen by the detector. The optical image was displayed

on the monitor as it was acquired, via the Nanoscope control software (v5.12), by connecting the photon counter output signal to an auxiliary port on the Nanoscope IV AFM controller.

**The dry imaging data acquisition system included 27 electronics boxes and several sets of software. This hard-wired system was not adaptable to wet imaging.**

A new Data Acquisition and Control (DAC) system was developed using National Instruments cards and LabView software. The flexibility of this system enabled the microscope to be adapted for imaging wet environments. A description of this DAC is provided in Appendix E.

**It was desirable to produce combined AFM-optical images that were easily interpreted by eye.**

Digital images are typically encoded in RGB. The difficulty with that is that the gray scale is entangled with the color information. An additional difficulty is that the eye is more sensitive to some colors (e.g. green) than to others (e.g. red). As a result, the grayscale must be changed after combining RGB encoded images. While doing so the user has a tendency to rebalance the image: to emphasize specific colors to be more esthetically pleasing. The result does not maintain data integrity.

Alternative method of encoding images is based on Hue, Saturation and Value (HSV). In this system all three components are independent. Hue is color. Saturation is the depth of the color. Value is grayscale. This system can be used to encode the AFM topographic image in value. Each of the emission spectral bands detected can be assigned a different hue. The saturation of that hue is the direct representation of intensity. Since each of these parameters are independent, co-localization is nicely accounted for in the color mathematics by assigning the appropriate intermediate hues. The specific hue can be assigned depending on the relative intensity of the two spectral

bands with the saturation representing the combined intensity. Other researchers can then disentangle the specific band intensities at each pixel without loss of information (2 variables, 2 knowns). Later, this image can be converted back to RGB for presentation. Data integrity is preserved by eliminating any need to rebalance the combined image.

HSV is presented in more detail in Appendix F.

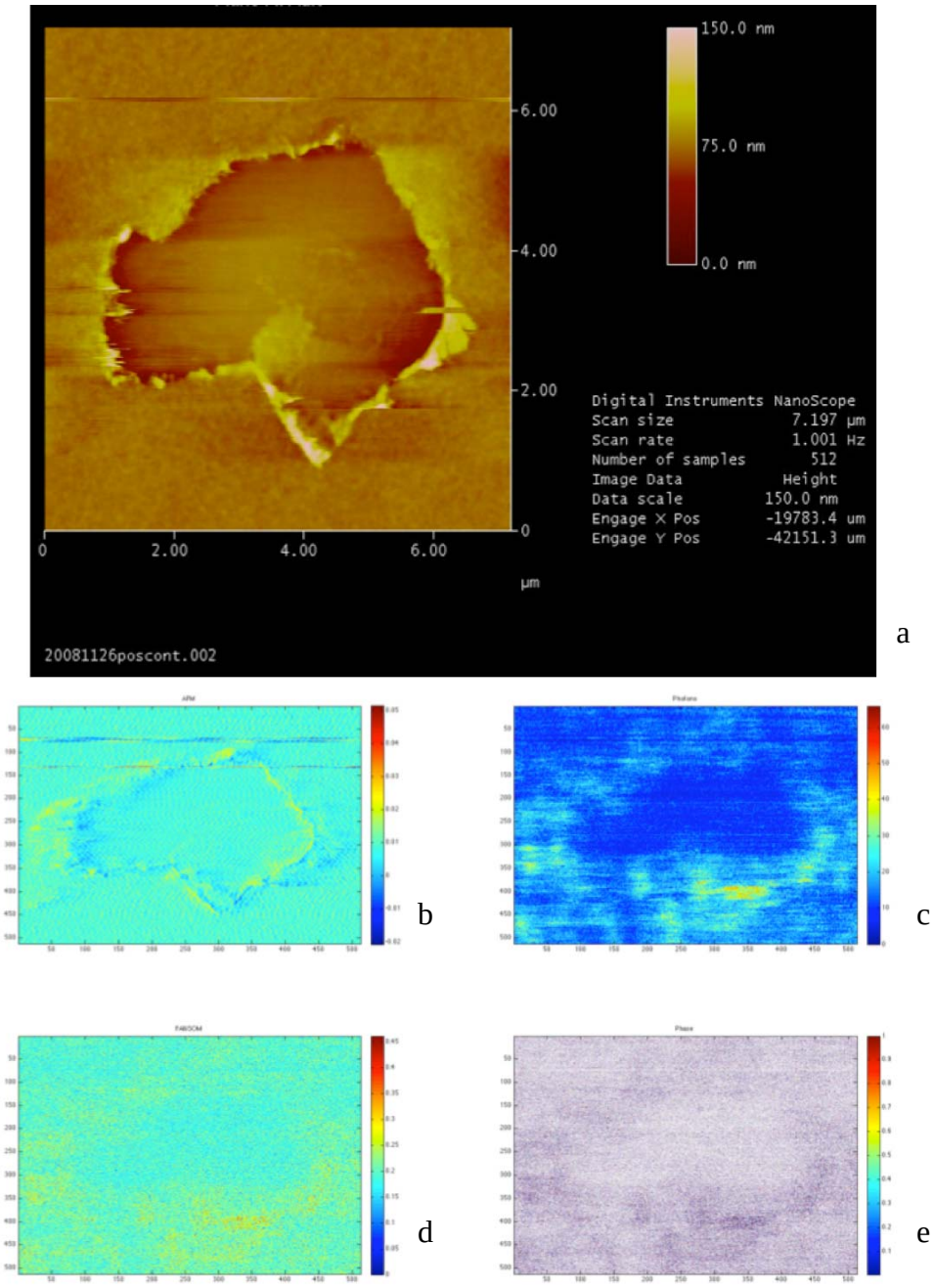


Figure 3.4 An AFM image of a wet membrane ghost from a N2a cell that was attached to a glass coverslip was generated using Veeco Nanoscope software. It was labeled by a mCherry tagged membrane-bound protein. b shows the AFM image computed by the Matlab image processing software we developed. The Matlab scripts for this software are given, in their entirety in Appendix E. c shows the total photon count and is essentially a normal TIRF image. d shows a near-field image computed using the same method described in the 2004 PRL by Gerton et al. e shows a vector summed image indicative of stimulated emission.

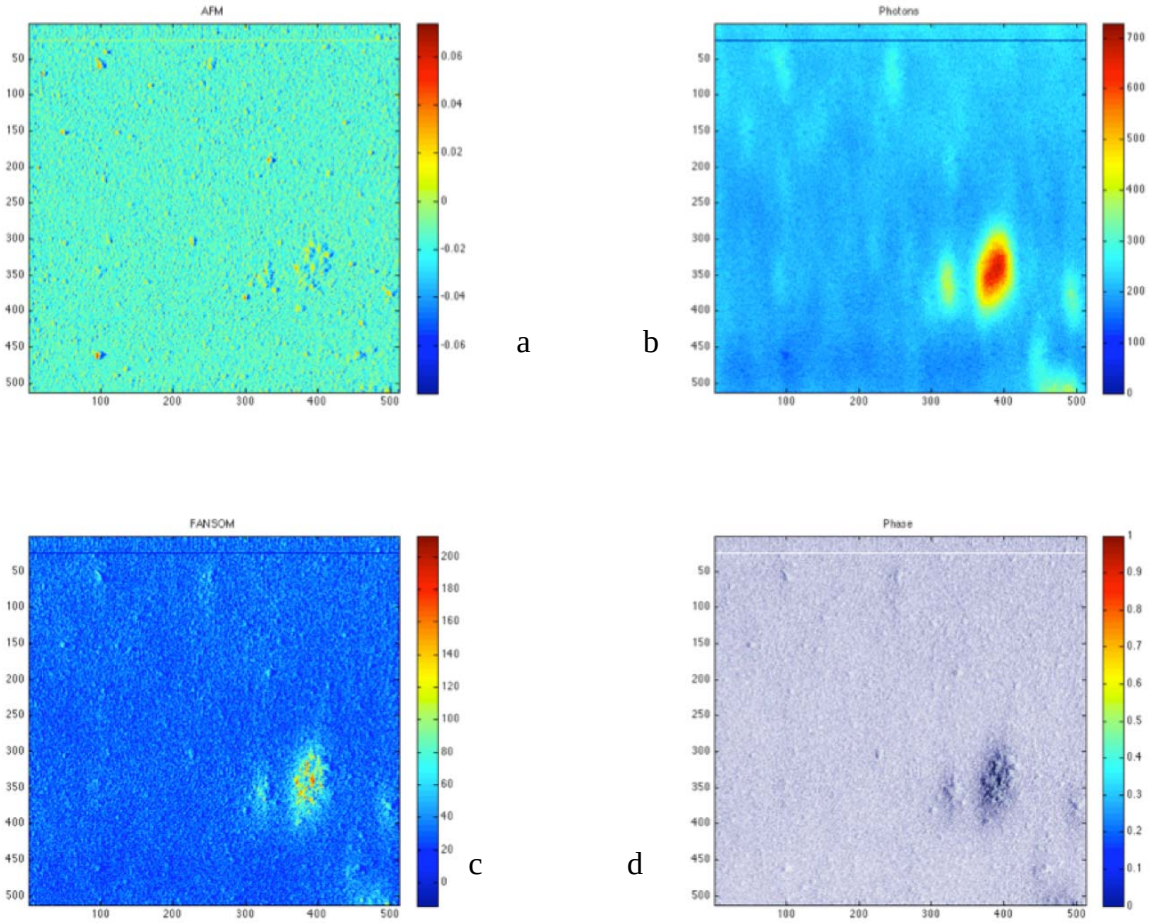


Figure 3.5 An AFM image computed by our Matlab image processing software (Appendix E) for a N2a cell transfected with α4 mCherry β2 wild type. b shows the total photon count and is essentially a normal TIRF image. c shows a fansom computed image using the same method described in the 2004 PRL by Gerton et al. d shows a vector summed image indicative of stimulated emission.

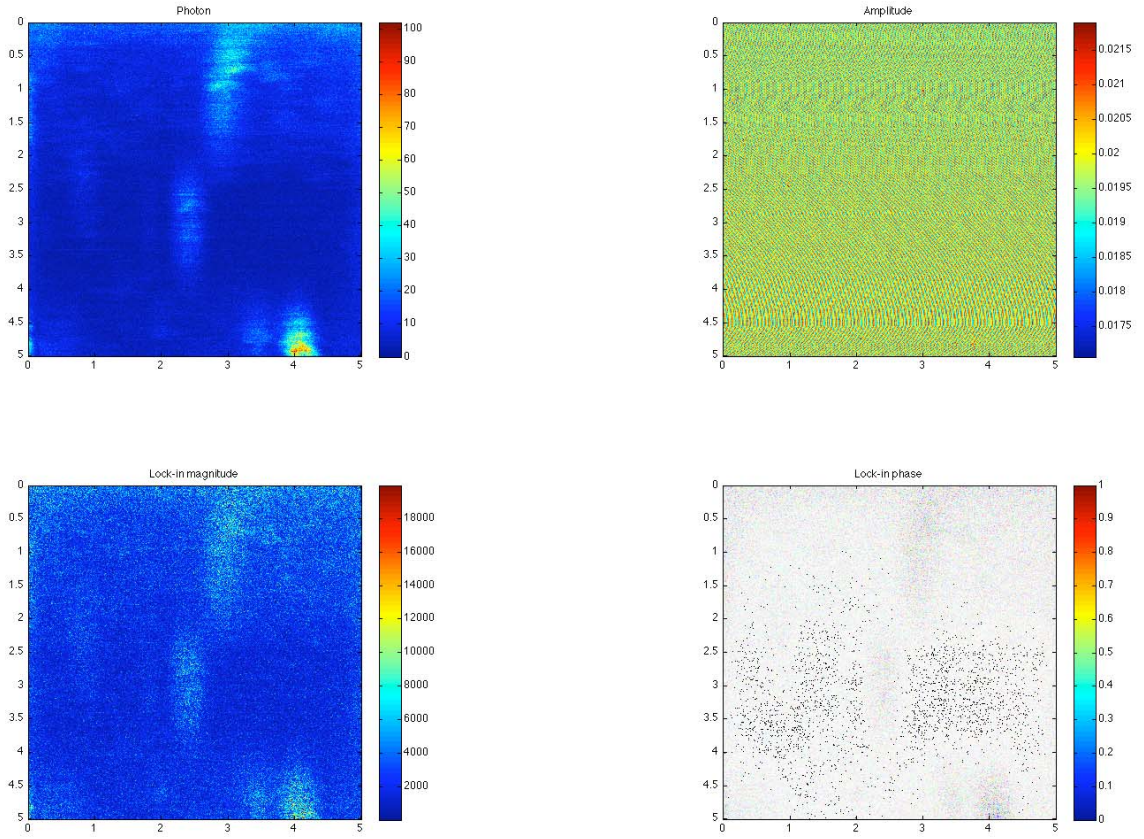


Figure 3.6 Measurement 20091106Wbd1. Top left is the AFM image computed by our Matlab image processing software (Appendix E) for extracellular fluid immersed 20 nm latex beads adhered to a class coverslip. The beads are labeled with red fluorescent dye. Top right is the total photon count image and is essentially a normal TIRF image. Bottom left shows a near-field image computed using the same method described in the 2004 PRL by Gerton et al. Bottom right is a vector summed near-field image indicative of stimulated emission. The FoV is 5 microns.

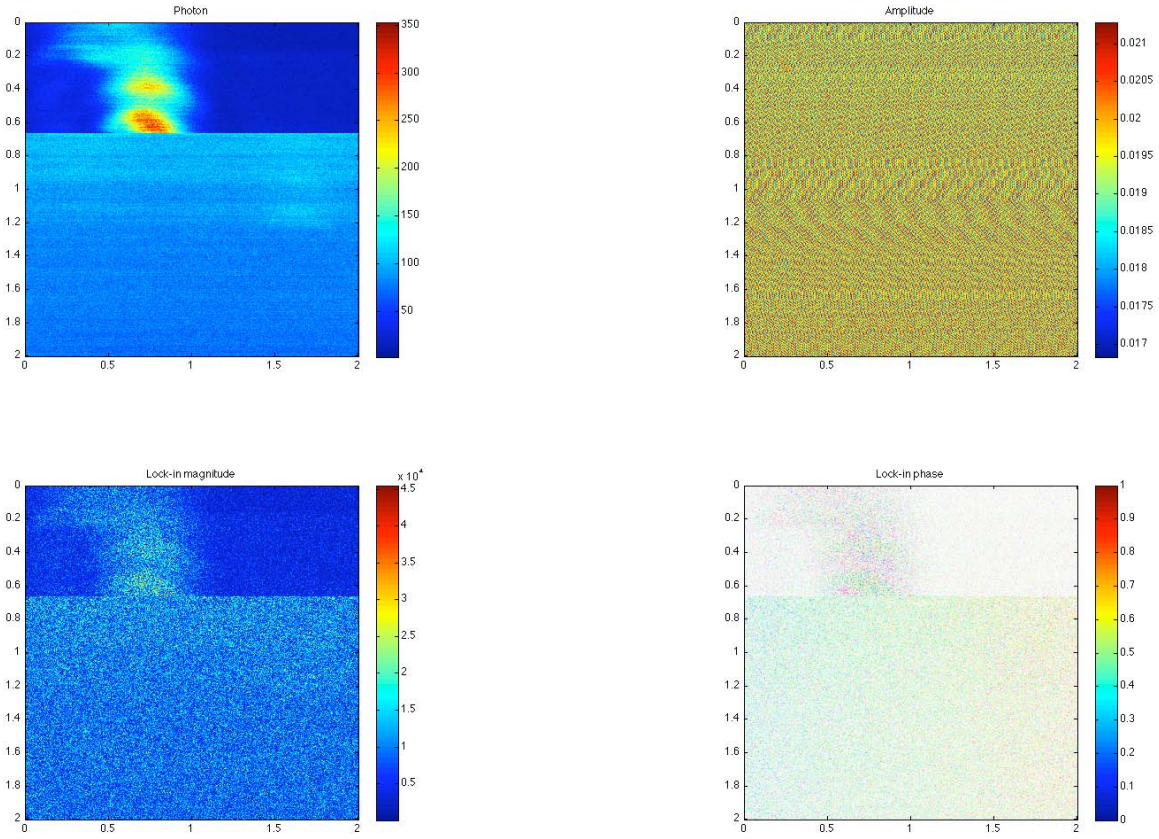


Figure 3.7 Measurement 20091106Wbd3. Top left is the AFM image computed by our Matlab image processing software (Appendix E) for 20 nm latex beads adhered to a class coverslip and immersed in extracellular liquid. The beads are labeled with red fluorescent dye. Top right is the total photon count image and is essentially a normal TIRF image. Bottom left shows a near-field image computed using the same method described in the 2004 PRL by Gerton et al. Bottom right is a vector summed near-field image indicative of stimulated emission. The FoV is 2 microns. Note that the image suddenly changes at 0.7 microns on the y-axis. That is because a bead stuck to the AFM tip partway though the image.

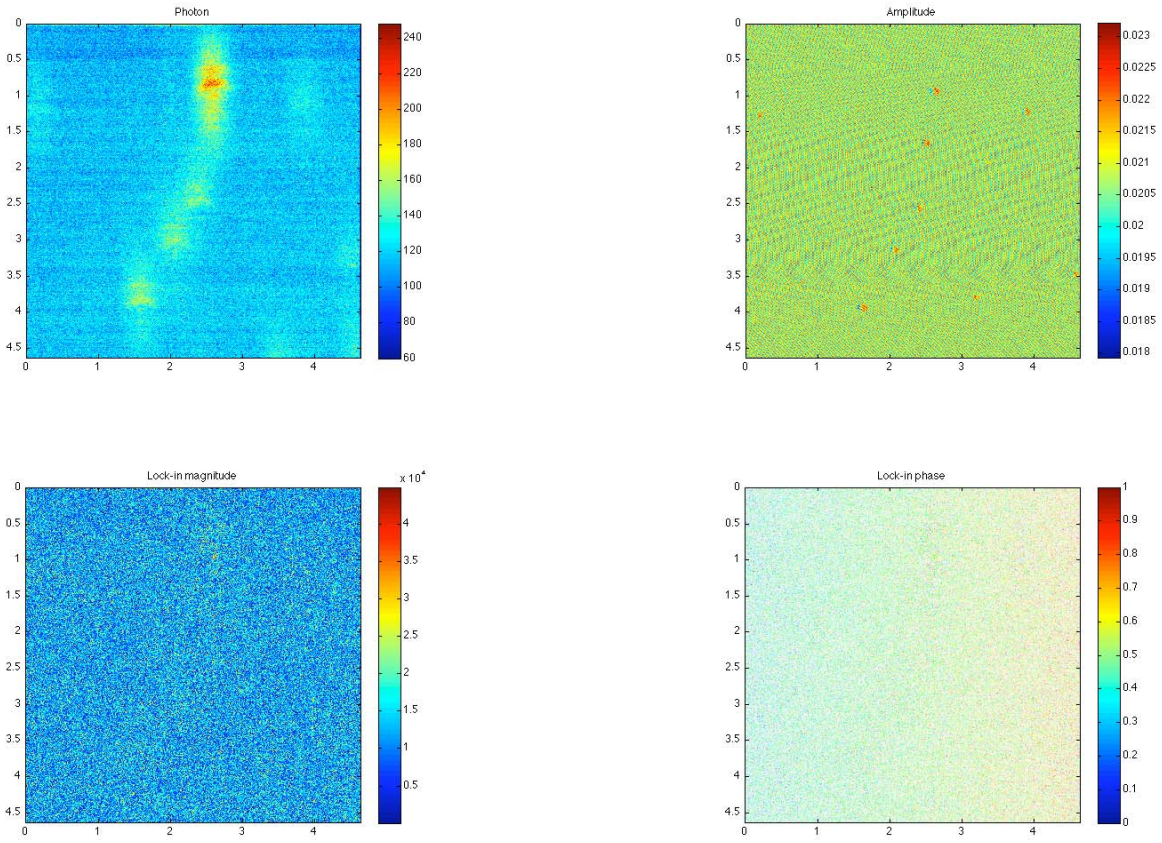


Figure 3.8 Measurement 20091106Wbd5. Top left is an AFM image computed by our Matlab image processing software (Appendix E) for extracellular fluid immersed 20 nm latex beads adhered to a class coverslip. The beads are labeled with Red fluorescent dye. Top right is the total photon count image and is essentially a normal TIRF image. Bottom left shows a near-field image computed using the same method described in the 2004 PRL by Gerton et al. Bottom right is a vector summed near-field image indicative of stimulated emission. The FoV is 4.6 microns.

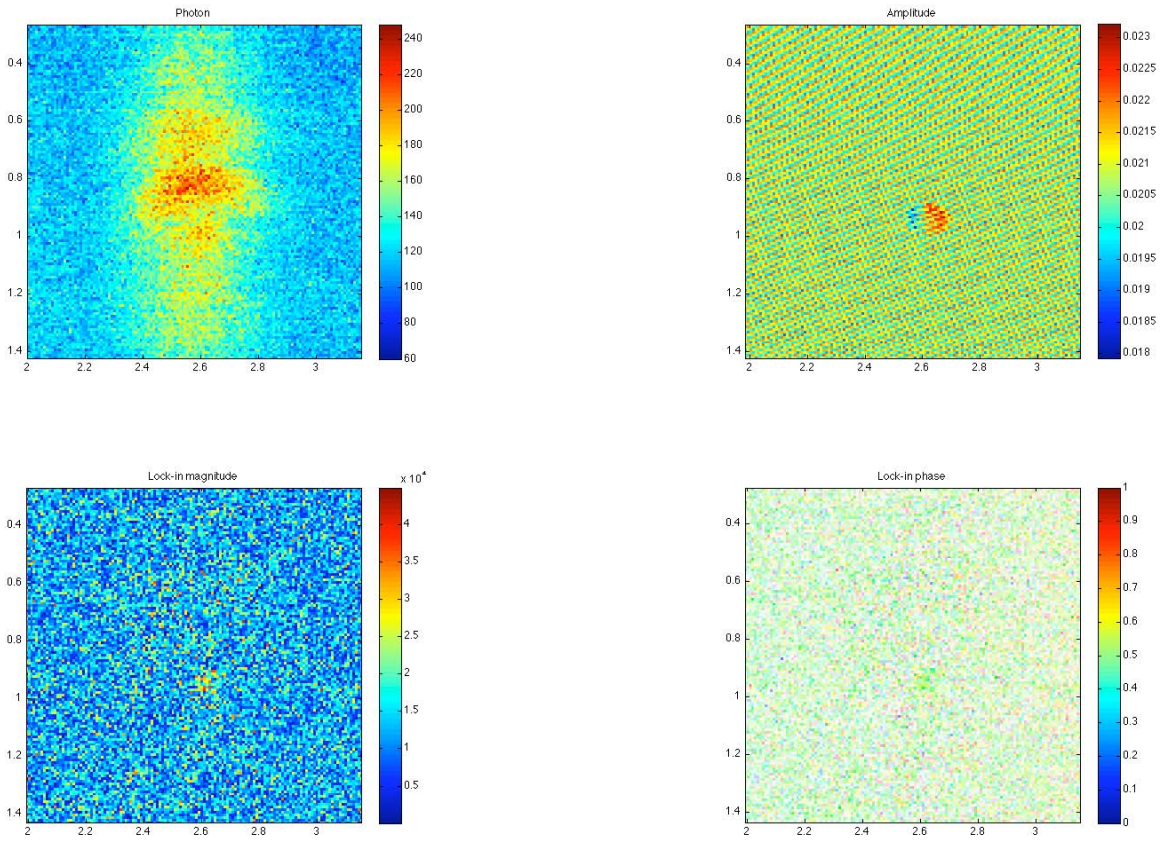


Figure 3.9 Measurement 20091106Wbd5 zoomed in to show a region ~1.2 microns across from Figure 3.6. Top left is a AFM image computed by our Matlab image processing software (Appendix E) for extracellular fluid immersed 20 nm latex beads adhered to a class coverslip. The beads are labeled with red fluorescent dye. Top right is the total photon count image and is essentially a normal TIRF image. Bottom left shows a near-field image computed using the same method described in the 2004 PRL by Gerton et al. Bottom right is a vector summed near-field image indicative of stimulated emission.

### 3.3 Summary and Conclusions

A TEFM was modified to enable imaging of wet samples. As examples a membrane ghost image is presented in Figure 3.2 and a typical cell image is presented in Figure 3.3. A second version of this microscope was built with greatly increased capability including simultaneous detection of two colors, excitation at three laser wavelengths in either of two modes of vertical polarization.

While many hundreds of cells and cell membrane ghosts were imaged during this effort the results were inconsistent. Figures 3.4-3.7 show images of 20 nm beads in extracellular solution. Clearly there is coupling between the tip and sample. What it means however is uncertain. Resolution of these inconsistencies will require careful study of the tip-laser interactions in water and cell media.

### Acknowledgements

After Stephen Quake left Caltech for a faculty position at Stanford, he committed to leave the TEFM at Caltech for the duration of the studies reported herein. This is a remarkable act of generosity for which I am very, very grateful. Thanks also go to Eyal Shafran (Un. Utah) and Daniel Lo (Caltech) for assistance with the detection software, David Kremmers for suggesting HSV for combining images, Jian Li (JPL) and Mike Gordon (UCSB) for assistance with the data acquisition software and Rob Sharrow for a great deal of help with both. Building the two color TEFM would have been impossible without the sage advice and craftsmanship of Mike Roy and Steve Olson of the Chemistry Department's Instrument shop. Finally, thanks to Paul Millman and Chroma Technology for quickly making custom filters of incredibly high quality. Funding from the JPL Research and Technology Development and BioNano programs, NASA-PRSGC IDEAS-ER grant, NIH, NSF, NS-11756, DA-17279, and the Philip Morris External Research Program is gratefully acknowledged.

## Reference


[1] Gerton, J. M., Wade, L. A., Lessard, G. A.. Ma, Z. and Quake, S. R., Tip-enhanced fluorescence microscopy at 10 nanometer resolution, *Phys. Rev. Lett.*, (2004) **93** 180801.

[2] Ma, Z., Gerton, J.M., Wade, L.A. and Quake, S.R., Fluorescence near-field microscopy of dna at sub-10 nm resolution, *Phys. Rev. Lett.* (2006) **97** 260801.

[3] Novotny, L., Bian, R. X. and Xie, X. S., Phys. Rev. Lett.(1997) **79** 645.

[4] Sanchez, E. J., Novotny, L. and Xie, X. S. Phys. Rev. Lett. (1999) **82** 4014.

[5] Novotny, L., J. Am. Cer. Soc. (2002) **85** 1057.

[6] Hamann, H. F., Gallagher, A. and Nesbitt, D. J., Appl. Phys. Lett. (1998) **73** 1469.

[7] Hillenbrand, R. and Keilmann, F. Appl. Phys. Lett. (2002) **80** 25.

[8] Hartschuh, A., Sanchez, E. J., Xie, X. S., and Novotny, L., Phys. Rev. Lett. (2003) **90** 0995503.

[9] Hamann, H. F., Kuno, M., Gallagher, A. and Nesbitt, D. J., J. Chem. Phys. (2001) **114** 8596.

[10] Protasenko,V.V., Kuno, M., Gallagher, A. and Nesbitt, D. J. Opt. Comm. (2002) **210** 11.

[11] Kramer, A., Trabesinger, W., Hecht, B. and Wild, U. P., Appl. Phys. Lett. (2002) **80** 1652.

[12] Bouhelier, A., Beversluis, M., Hartschuh, A. and Novotny, L. Phys. Rev. Lett. (2003) **90** 013903.

[13] Sick, B., Hecht, B., Wild, U. P. and Novotny, L., J. Micr. (2001) **202** 365.

[14] Yang, T. J., Lessard, G. A. and Quake, S. R., Appl. Phys. Lett. (2000) **76** 378.

[15] Closed-Look Bioscope with Nanoscope IV controller, Veeco Metrology, 112 Robin Hill Road, Santa Barbara, CA 93117, USA.

[16] nPoint closed-loop AFM scanner, pn iCXY100LA-BO with nPoint C300 DSP Controller. nPoint, 3030 Laura Ln Suite 100, Middleton, WI 53562 USA.

[17] Olympus UPlanFl 100x/1.30 Oil. Olympus America Inc., 3500 Corporate Parkway, Center Valley, PA, USA

[18] Zeiss $\alpha$ Plan-Fluar 100x/1.45 Oil, pn 000000-1084-514. Carl Zeiss MicroImaging, Inc., One Zeiss Drive, Thornwood, NY 10594, USA.

[19] Veeco Direct Drive Fluid Cantilever Holder, pn 013-410-000. Veeco Metrology, 112 Robin Hill Road, Santa Barbara, CA 93117, USA.

[20] MatTek pn P50G-0-30F. MatTek Corporation, 200 Homer Avenue, Ashland, MA 01721, USA.

[21] Nanosensors, Rue Jaquet-Droz 1, Case Postale 216, CH-2002 Neuchatel, Switzerland.

[22] Thorlabs pn CPS186. Thorlabs, Newton, New Jersey, USA.

[23] ARCopix Radial Polarization Converter with USB ARCoptix LC driver. ARCotix S.A., Rue de la Maladiere 71, 2000, Neuchatel, NE, Switzerland.

[24] Chroma Technology Corp. • 10 Imtec Lane • Bellows Falls, VT 05101 USA.

[25] SRS400 Gated Photon Counter. Stanford Research Systems, Inc., 1290-D Reamwood Ave., Sunnyvale, CA 94089, USA.